

Supplementary Information

High-quality All-inorganic Perovskite CsPbBr₃ Microsheet Crystals as Low-loss Subwavelength Exciton–Polariton Waveguides

Zijuan Li^{1, #}, Fengsheng Sun^{1, #}, Zebo Zheng^{1, #}, Jun Chen¹, Albert V. Davydov², Shaozhi Deng^{1, *}, Huairuo Zhang^{2, 3, *}, Huanjun Chen^{1, *}, Fei Liu^{1, *}

¹State Key Laboratory of Optoelectronic Materials and Technologies, Guangdong Province Key Laboratory of Display Material and Technology, and School of Electronics and Information Technology, Sun Yat-sen University, Guangzhou 510275, China

² Materials Science and Engineering Division, National Institute of Standards and Technology, Gaithersburg, MD 20899, USA

³ Theiss Research, Inc., La Jolla, CA 92037, USA

*Corresponding email: liufei@mail.sysu.edu.cn, chenhj8@mail.sysu.edu.cn, huairuo.zhang@nist.gov, stdsz@mail.sysu.edu.cn

[#]These authors contributed equally to this paper.

1. Methods

Synthesis of CsPbBr₃ microsheets: CsBr (Aladdin Inc., 99.999%) and PbBr₂ (Aladdin Inc., 99.999%) powders were used as the precursors, whose molar ratio is controlled at 1:1 for the formation of high-quality CsPbBr₃ single crystals. The source materials were placed at both ends of an alumina boat and inserted into the central region of a tube furnace. Subsequently, a mica substrate was placed in the high-temperature region, at a distance of several centimeters from the alumina boat. During the growth process, Ar gas was used as the protection gas and the reaction pressure was kept at 760 Torr. After a growth of 0.5-1 h at 650 °C, a yellow film was found on the surface of the mica substrate.

Morphology and size control of the CsPbBr₃ microsheets: A schematic diagram of the ambient-pressure growth of the CsPbBr₃ microsheets is shown in Figure S1(a). Specifically, mica was employed as the substrate, which can be divided into the right (*R*), middle (*M*), and left (*L*) regions along the air flow direction. Typical morphologies of the products are provided in Figure S1(b)-1(d). The density of the microsheets gradually decreases from 81 mm⁻² to 59 mm⁻² and their average size ranges from 150 μm to 100 μm along the gas flow direction. The mean thickness of the microsheets gradually decreases from 900 nm to 140 nm as the distance between the substrate and the sources increases. The microsheets all exhibit rectangular shapes and smooth edges in all three regions of the mica substrate, suggesting their good crystallinity. The growth mechanism of the CsPbBr₃ microsheets on the mica substrate under ambient pressure can be ascribed to the epitaxial growth induced by van der Waals (vdW) forces, as reported in previous studies.¹⁻¹⁰ Based on this mechanism, the orthorhombic CsPbBr₃ microsheets tend to form on the mica substrate with a vdW layered structure at temperatures above 620 °C. The nonuniform surface of the mica substrate is likely responsible for their different sizes and thicknesses. In our experiments, two major factors determine the morphology of the CsPbBr₃ structures: the growth temperature and the distance between the sources and substrate. The mean edge length of the CsPbBr₃ microsheets sharply increases from 20 μm to 300 μm when the growth temperature is raised from 620 °C to 650 °C, which is attributed to the favorable formation of higher densities of microsheets at elevated temperatures. However, when the temperature is lower than 600 °C, CsPbBr₃ microsheets cannot be formed, and only nanoparticles are found on the surface of the mica wafer. As shown in Figure S1, the average size and growth density of the microsheets decrease with increasing evaporation distance. The precursor concentration decreases with increasing evaporation distance, leading to a reduction in the nuclei density based on the vdW growth mechanism.

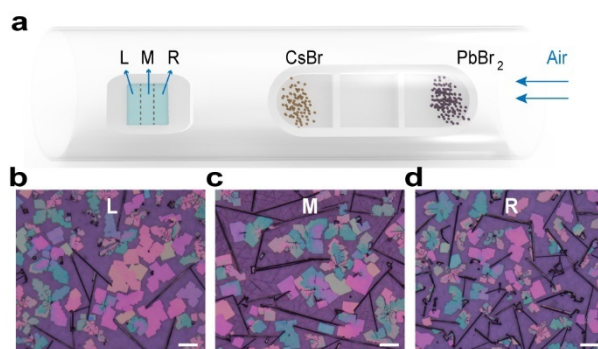


Fig. S1 **a** Schematic diagram of the growth of the CsPbBr₃ microsheets. *L*: left region; *M*: middle region; *R*: right region. **b-d** Typical optical images of the CsPbBr₃ microsheets, corresponding to the right, middle, and left regions of the mica substrate, respectively. Scale bars are 100 μ m.

Characterization: AFM (Dimension FastScan, Bruker) and optical microscopy (BX43, Olympus) were applied to observe the morphology of the products. XRD (D-MAX 2200 VPC, Rigaku), XPS (ESCALAB 250Xi, Thermo Fisher) and probe-corrected STEM (Titan3 80-300, FEI) were used to ascertain their chemical compositions and crystal structure. Time-resolved PL (FLSP920, Edinburgh Instruments LTD) measurements were conducted to investigate the carrier lifetime of the microsheet samples, where the picosecond pulsed diode laser (EPL-405) with a wavelength of 406.2 nm and a pulse width of 58.8 ps was used as the excitation source. The bandgap of the product was determined by ultraviolet-visible (UV-Vis) spectroscopy (U-3900, Hitachi) and PL spectroscopy (InVia-Reflex, Renishaw).

To prepare thin microsheet samples with thicknesses of less than 30 nm for TEM characterizations, the as-grown samples are dispersed into ethanol solution and milled in the corundum crucible for 10 min. Afterwards, the suspension was deposited onto TEM grid for atomic resolution imaging. The HAADF STEM image of the microsheet was obtained along the [100] zone axis.

The near-field optical measurements were conducted using a commercially available s-SNOM (NeaSNOM, Neaspec GmbH). To image the exciton-polariton waves, the laser (532 nm, Oxxius; 633 nm, Thorlabs; 785 nm, Toptica; 1064 nm and 1550 nm, RIO Orion) was focused onto the microsheet sample through a metal-coated AFM tip (Arrow-IrPt, NanoWorld). The tip was vibrated vertically with a frequency of 280 kHz. The back-scattered light from the tip is collected by a detector (PDA20CS-EC, Thorlabs), and the optical signal was demodulated in a pseudoheterodyne interferometric manner. The third harmonics of the s-SNOM signal is used in our study (Fig. S6).

2. Solutions of transverse magnetic (TM) and transverse electric (TE) waveguide modes

The propagation of electromagnetic wave should satisfy the Maxwell's equations,

$$\begin{cases} \nabla \times \vec{E} = -i\omega\mu_0\vec{H}, \\ \nabla \times \vec{H} = i\omega\epsilon_0\epsilon_m\vec{E}. \end{cases} \quad (S1)$$

A typical 2D waveguide mode with an in-plane propagation wave vector of \vec{q} can be expressed as $\vec{E}(x, z, t) = \vec{e}E(z)\exp(iqx - i\omega t)$ or $\vec{H}(x, z, t) = \vec{e}H(z)\exp(iqx - i\omega t)$, where \vec{e} is the unit vector of the electromagnetic field. For isotropic materials, the Maxwell's equations have two independent solutions which are expressed as,

$$\begin{cases} \frac{\partial H_x}{\partial z} - iqH_z = i\omega\epsilon_0\epsilon_m E_y, \\ \frac{\partial E_y}{\partial z} = i\omega\mu_0 H_x, \\ iqE_y = -i\omega\mu_0 H_z. \end{cases} \quad (TE), \quad \begin{cases} \frac{\partial E_x}{\partial z} - iqE_z = -i\omega\mu_0 H_y, \\ -\frac{\partial H_y}{\partial z} = i\omega\epsilon_0\epsilon_m E_x, \\ iqH_y = i\omega\epsilon_0\epsilon_m E_z. \end{cases} \quad (TM). \quad (S2)$$

By organizing the above equation, we can obtain the expressions of the electromagnetic fields of TM and TE waves in material as,

$$\begin{cases} \frac{\partial^2 E_y}{\partial z^2} + (k_0^2\epsilon_m - q^2)E_y = 0, & (TE) \\ \frac{\partial^2 H_y}{\partial z^2} + (k_0^2\epsilon_m - q^2)H_y = 0, & (TM) \end{cases} \quad (S3)$$

where ϵ_m is the dielectric constant of isotropic material and parameter $k_0 = \omega\sqrt{\epsilon_0\mu_0}$ is the free-space wavevector. Because the waveguide modes are confined to the two interfaces, the electric and magnetic fields for the TM (E_x, H_y, E_z) modes should have the forms as,

$$H_y = \begin{cases} A\exp(-\alpha_z z), & z \geq 0 \\ A\cos(k_z z) + B\sin(k_z z), & -d < z < 0 \\ [A\cos(k_z d) - B\sin(k_z d)]\exp[\alpha_s(z + d)], & z \leq -d \end{cases} \quad (S4)$$

$$E_x = \begin{cases} -\frac{i\alpha_c}{\omega\epsilon_0\epsilon_c} A \exp(-\alpha_c z), & z \geq 0 \\ -\frac{ik_z}{\omega\epsilon_0\epsilon} [A \sin(k_z z) - B \cos(k_z z)], & -d < z < 0 \\ \frac{i\alpha_s}{\omega\epsilon_0\epsilon_s} [A \cos(k_z d) - B \sin(k_z d)] \exp[\alpha_s(z+d)], & z \leq -d \end{cases} \quad (S5)$$

$$E_z = \begin{cases} \frac{q}{\omega\epsilon_0\epsilon_c} A \exp(-\alpha_c z), & z \geq 0 \\ \frac{q}{\omega\epsilon_0\epsilon} [A \sin(k_z z) - B \cos(k_z z)], & -d < z < 0 \\ \frac{q}{\omega\epsilon_0\epsilon_s} [A \cos(k_z d) - B \sin(k_z d)] \exp[\alpha_s(z+d)], & z \leq -d \end{cases} \quad (S6)$$

where d is the thickness of the 2D waveguide layer, ϵ_c , ϵ and ϵ_s are dielectric constants of cover (Air), waveguide (CsPbBr₃), and substrate (Mica) layers, respectively. And parameters $\alpha_{c,s} = \sqrt{q^2 - k_0^2 \epsilon_{c,s}}$ and $k_z = \sqrt{k_0^2 \epsilon - q^2}$. The solutions of the TM (E_x , H_y , E_z) modes can be obtained by matching the boundary conditions at the interfaces ($z = 0$ and $z = -d$) as,

$$\begin{cases} E_x^{(c)} = E_x^{(w)}, & H_y^{(c)} = H_y^{(w)} & (z = 0) \\ E_x^{(w)} = E_x^{(s)}, & H_y^{(w)} = H_y^{(s)} & (z = -d) \end{cases} \quad (S7)$$

where the superscripts “c”, “w”, and “s” represent the cover (Air), waveguide (CsPbBr₃), and substrate (Mica) layers, respectively. Then we can obtain

$$\begin{pmatrix} \frac{\alpha_c}{\epsilon_c} & \frac{k_z}{\epsilon} \\ \frac{k_z}{\epsilon} \sin(k_z d) - \frac{\alpha_s}{\epsilon_s} \cos(k_z d) & \frac{k_z}{\epsilon} \sin(k_z d) + \frac{\alpha_s}{\epsilon_s} \cos(k_z d) \end{pmatrix} \begin{pmatrix} A \\ B \end{pmatrix} = 0. \quad (S8)$$

Consequently, the exciton-polariton TM modes in the waveguide and the associated dispersion relations can be obtained by solving the equation (S8). Specifically, the dispersion relation can be stated as,

$$d\sqrt{k_0^2 \epsilon - q^2} = \tan^{-1} \left(\frac{\epsilon}{\epsilon_c} \sqrt{\frac{q^2 - k_0^2 \epsilon_c}{k_0^2 \epsilon - q^2}} \right) + \tan^{-1} \left(\frac{\epsilon}{\epsilon_s} \sqrt{\frac{q^2 - k_0^2 \epsilon_s}{k_0^2 \epsilon - q^2}} \right) + m\pi, \quad (S9)$$

with $m = 0, 1, 2, \dots$ the orders of the TM modes.

The electric and magnetic fields of the TE (H_x , E_y , H_z) modes should have the forms as,

$$E_y = \begin{cases} C \exp(-\alpha_c z), & z \geq 0 \\ C \cos(k_z z) + D \sin(k_z z), & -d < z < 0 \\ [C \cos(k_z d) - D \sin(k_z d)] \exp[\alpha_s (z + d)], & z \leq -d \end{cases} \quad (\text{S10})$$

$$H_x = \begin{cases} -\frac{i\alpha_c}{\omega\mu_0} C \exp(-\alpha_c z), & z \geq 0 \\ -\frac{ik_z}{\omega\mu_0} [C \sin(k_z z) - D \cos(k_z z)], & -d < z < 0 \\ \frac{i\alpha_s}{\omega\mu_0} [C \cos(k_z d) - D \sin(k_z d)] \exp[\alpha_s (z + d)], & z \leq -d \end{cases} \quad (\text{S11})$$

$$H_z = \begin{cases} -\frac{q}{\omega\mu_0} C \exp(-\alpha_c z), & z \geq 0 \\ -\frac{q}{\omega\mu_0} [C \sin(k_z z) + D \cos(k_z z)], & -d < z < 0 \\ -\frac{q}{\omega\mu_0} [C \cos(k_z d) - D \sin(k_z d)] \exp[\alpha_s (z + d)], & z \leq -d \end{cases} \quad (\text{S12})$$

The solutions of the TE (H_x, E_y, H_z) modes can be obtained by matching the boundary conditions at the interfaces ($z = 0$ and $z = -d$) as,

$$\begin{cases} H_x^{(c)} = H_x^{(w)}, & E_y^{(c)} = E_y^{(w)} & (z = 0) \\ H_x^{(w)} = H_x^{(s)}, & E_y^{(w)} = E_y^{(s)} & (z = -d) \end{cases} \quad (\text{S13})$$

Then we can obtain

$$\begin{pmatrix} \alpha_c & k_z \\ k_z \sin(k_z d) - \alpha_s \cos(k_z d) & k_z \sin(k_z d) + \alpha_s \cos(k_z d) \end{pmatrix} \begin{pmatrix} C \\ D \end{pmatrix} = 0. \quad (\text{S14})$$

Consequently, the exciton-polariton TE modes in the waveguide and the associated dispersion relations can be obtained by solving the equation (S14). Specifically, the dispersion relation can be stated as,

$$d\sqrt{k_0^2 \varepsilon - q^2} = \tan^{-1} \left(\sqrt{\frac{q^2 - k_0^2 \varepsilon_c}{k_0^2 \varepsilon - q^2}} \right) + \tan^{-1} \left(\sqrt{\frac{q^2 - k_0^2 \varepsilon_s}{k_0^2 \varepsilon - q^2}} \right) + n\pi, \quad (\text{S15})$$

where $n = 0, 1, 2, \dots$ is the orders of the TE modes.

3. Crystallographic characterization of CsPbBr₃ microsheets

A typical XRD pattern of the as-grown CsPbBr₃ microsheets is presented in Figure S2, in which all the diffraction peaks of the sample are in good agreement with the orthorhombic *Pnma* structure. Moreover, very strong {200} and {202} diffraction peaks exist in this pattern, and their FWHM is narrow ($\approx 0.2^\circ$), revealing they are high-quality single crystals.

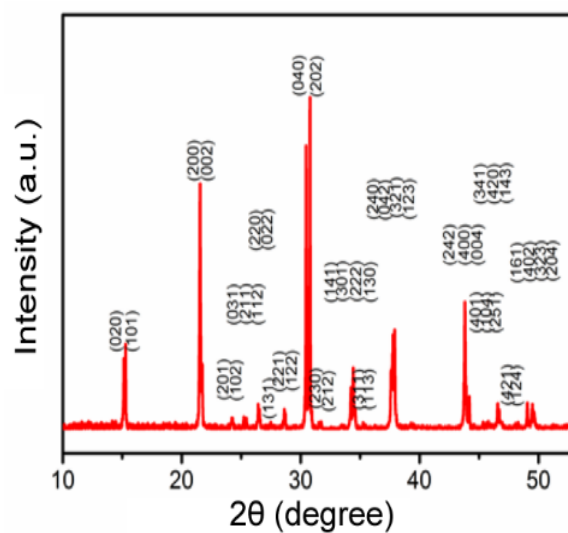


Fig. S2 Typical XRD pattern of the CsPbBr₃ microsheets.

4. Calculation of the exciton emission lifetime of the CsPbBr₃ microsheet film

For the time-resolved PL spectrum measurements, a pulsed ($\Delta t = 58.7$ ps) laser with a wavelength of 406.2 nm was chosen as the excitation source. To accurately calculate the exciton emission lifetime of the CsPbBr₃ microsheets, we provide their time-resolved PL decay curves in Figure S3, which were acquired from different sets of microsheets.

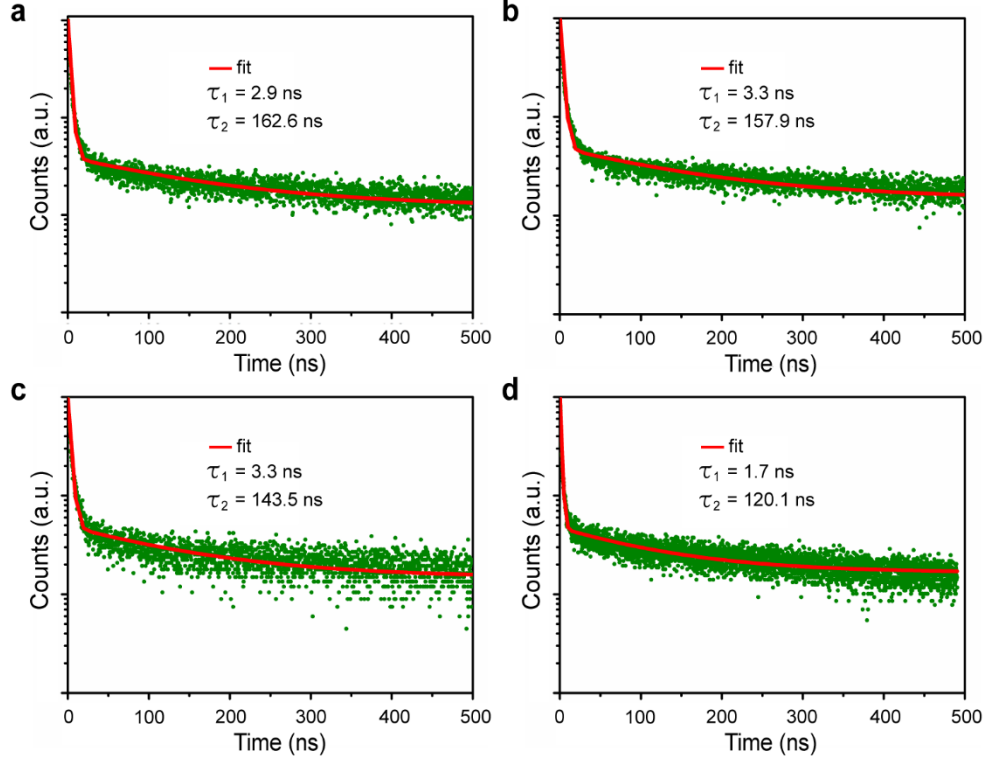


Fig. S3 PL decay curves and corresponding biexponential fitting results for microsheets under 406.2 nm irradiation in different regions of the same sample.

The exciton lifetime can be derived by the time-dependent biexponential equation:^{11, 12}

$$f(t) = f_1 e^{-t/\tau_1} + f_2 e^{-t/\tau_2} \quad \text{S(16)}$$

In Eq. S(16), f_1 and f_2 are constants representing the distribution coefficients, τ_1 and τ_2 represent the recombination times of the photogenerated surface carriers and bulk carriers, respectively, and t is the lifetime of the electron-hole pairs. From Eq. S(1), the fitting results of the PL decay curves from different regions of the sample can be obtained, as summarized in Table S1. The fitting uncertainty of all theoretical curves is better than 97.5%. The average exciton emission lifetimes (τ_{ave}) for different fitting curves can be determined by the expression $\tau_{ave} = \frac{\sum f_i \tau_i^2}{\sum f_i \tau_i}$. Based on this equation, all the slow decay characteristic times (τ_2) for different samples are deduced to be longer than 119 ns.

Table S1. Summary of the exciton emission lifetimes of CsPbBr₃ materials fabricated by different

approaches. QDs: quantum dots, NCs: nanocrystals, NPs: nanoparticles, NWs: nanowires.

Sample	τ_1 (ns)	τ_2 (ns)	τ_{ave} (ns)	Reference
CsPbBr ₃ QDs	/	/	9.72	12
CsPbBr ₃ QDs	1.43	6.35	5.14	13
CsPbBr ₃ QDs	/	/	4.81–6.41	14
CsPbBr ₃ NCs	/	/	7	15
CsPbBr ₃ film	2.43	20.24	10.02	16
CsPbBr ₃ NPs	/	/	15.1	17
CsPbBr ₃ NWs	/	/	2.5–20.6	18
CsPbBr₃ microsheets (sample I)	3.7	119.1	107.9	This work (main text)
CsPbBr₃ microsheets (sample II)	2.9	162.6	101.5	This work
CsPbBr₃ microsheets (sample III)	3.3	157.9	100.3	This work
CsPbBr₃ microsheets (sample IV)	3.3	143.5	78.3	This work
CsPbBr₃ microsheets (sample V)	1.7	120.0	79.8	This work

To better evaluate the waveguide behavior of the CsPbBr₃ microsheets, a comparison table of CsPbBr₃ materials fabricated by different methods is given in Table S1. The CsPbBr₃ microsheets produced by our method exhibit an extralong average exciton lifetime (τ_{ave}) of over 78 ns, which is longer than that of most of the CsPbBr₃ structures produced by other methods.¹²⁻¹⁸ It proves that the CsPbBr₃ microsheets fabricated by our one-step ambient-pressure CVD method should have enough high-quality crystallinity.

5. TE and TM modes of the CsPbBr₃ waveguides with different thicknesses

To find the optimal thickness of the CsPbBr₃ microsheet for waveguide applications, the dispersion relations of the CsPbBr₃ waveguides with different thicknesses are compared. As shown in Figure S4, the mode numbers of both the TE and TM modes increase as the thickness of the CsPbBr₃ microsheets increases. When the thickness of the CsPbBr₃ microsheets increases from 100 nm to 500 nm, the number of TE (TM) modes increases from 1 to 5. When the high-order TE and TM modes are permitted for thicker CsPbBr₃ microsheets, the incident free-space light can be more effectively confined inside the CsPbBr₃ waveguides to propagate at the nanoscale. Therefore, thicker CsPbBr₃ microsheets are proposed to be more suitable for visible-light waveguides.

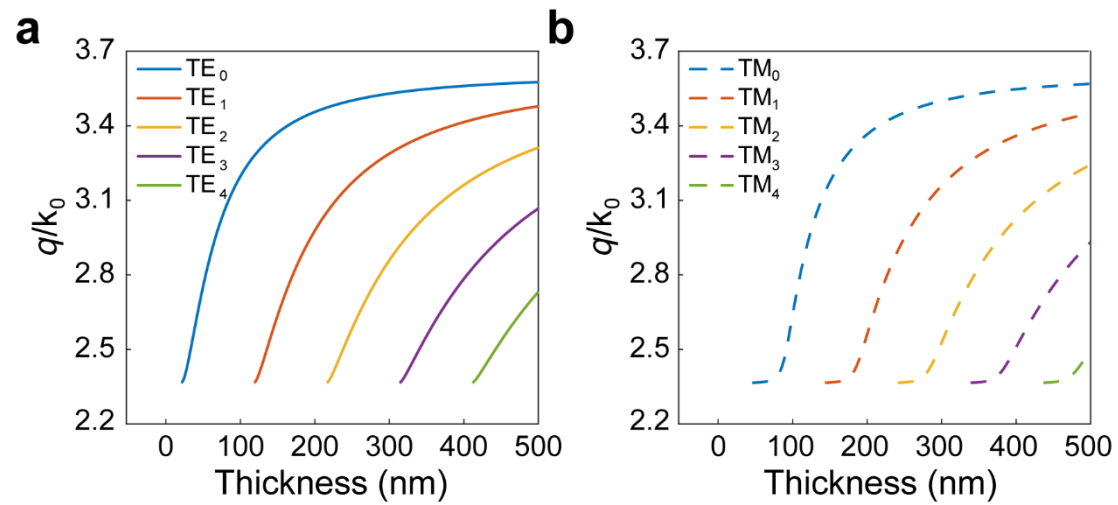


Fig. S4 a, b Thickness-dependent dispersion relations for the TE and TM modes of the CsPbBr₃ microsheet waveguide, respectively. The calculations are performed at a wavelength of 532 nm.

6. Propagation length of the CsPbBr₃ microsheet waveguides at different excitation wavelengths

To demonstrate the effect of the excitation wavelength on the propagation length of the CsPbBr₃ planar waveguide, Figure S5 shows s-SNOM images of a CsPbBr₃ microsheet under 633 nm and 532 nm irradiation. In these experiments, the angle between the incident light and the x - y plane is approximately 90°, and the thickness of the CsPbBr₃ microsheet is approximately 140 nm. Based on the calculation results shown in Figure S4, only the TE₀ and TM₀ modes are permitted for the 140-nm-thick microsheets. The intensity of the fringes gradually decreases when moving away from the sample edge for this sample at the two different irradiation wavelengths. When the irradiation wavelength (λ_0) is changed from 633 nm to 532 nm, the fringe spacing of the microsheets decreases from 0.61 μm to 0.35 μm . The OPD decreasing with the excitation wavelength is reasonable based on Eqs. (3) and (4) in the main text, in good accordance with the reported results.¹⁹ Most interestingly, the propagation length (d) will sharply increase from 16 μm to over 30 μm when the excitation wavelength decreases from 633 nm to 532 nm due to the emergence of the EP effect under 532 nm irradiation. This result is predicted by the calculation results of the electromagnetic field distribution for CsPbBr₃ waveguides (Figure 3). The results suggests that the CsPbBr₃ microsheets have extralong propagation distance over many other nanoscale waveguiding materials.

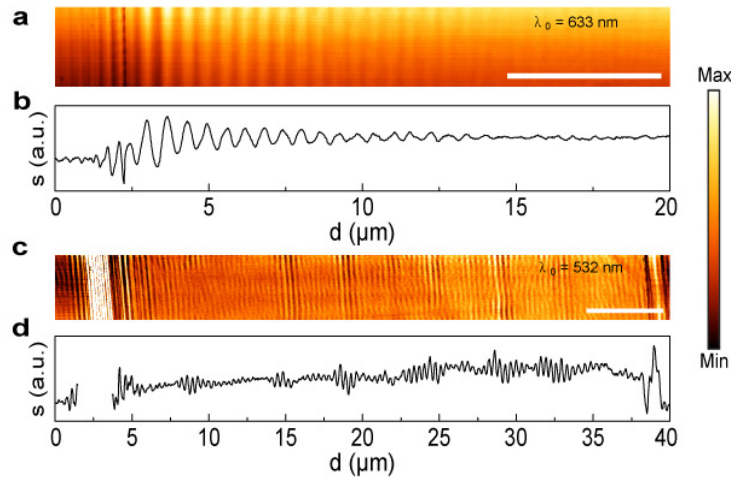


Fig. S5 **a, c** Representative s-SNOM images and near-field optical intensity distributions of the 173-nm-thick and 112-nm-thick CsPbBr₃ samples under 633-nm and 532-nm irradiations. **b, d** Corresponding near-field intensity profiles (s) along the propagation direction. Scale bars are 5 μm .

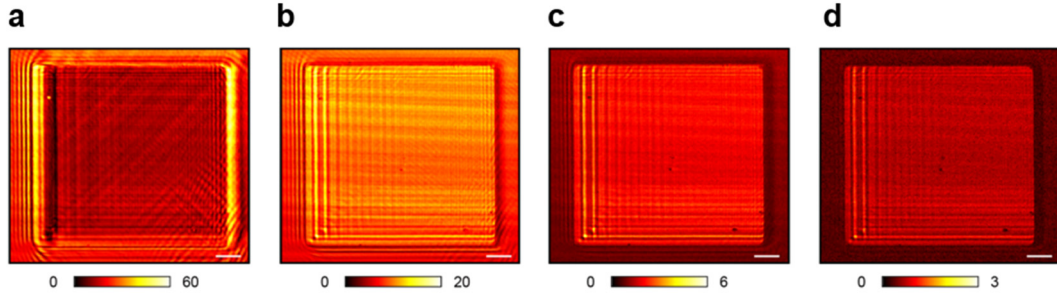


Fig. S6 S-SNOM images demodulated at (a) 1st harmonic, (b) 2nd harmonic, (c) 3rd harmonic, and (d) 4th harmonic of the vibration frequency of the AFM tip. Scale bars are 2 μm . The excitation wavelength is 532 nm. In the first harmonic signal (a), the intensity of background is strong, which will obscure the analysis of the exciton–polaritons. It can be found that the spatial distributions of light field in the second, third, and fourth harmonics are the same (b-d). However, the intensity will be lower for higher harmonic signals. Moreover, the fourth harmonics will fade away as the metallic tip is scanned for a long period of time. Therefore, the third harmonic signal is chosen in the study.

Table S2. Summary of the fitting parameters for PL spectra using the biexponential functions.

Figure No.	τ_1 (ns)	f_1	τ_2 (ns)	f_2	R_2
Figure 1h	3.7	40072	119.1	11484	0.99521
Figure S3a	2.9	1924	162.6	55	0.99095
Figure S3b	3.3	1943	157.9	68	0.9897
Figure S3c	3.3	610	143.5	22940	0.97531
Figure S3d	1.7	1299	120.1	39	0.98533

References

- (1) Zhang, Q.; Su, R.; Liu, X.; Xing, J.; Sum, T. C.; Xiong, Q. High-quality whispering-gallery-mode lasing from cesium lead halide perovskite nanoplatelets. *Adv. Funct. Mater.* **2016**, *26* (34), 6238–6245.
- (2) Hu, X.; Zhou, H.; Jiang, Z.; Wang, X.; Yuan, S.; Lan, J.; Fu, Y.; Zhang, X.; Zheng, W.; Wang, X.; Zhu, X.; Liao, L.; Xu, G.; Jin, S.; Pan, A. Direct vapor growth of perovskite CsPbBr₃ nanoplate electroluminescence devices. *ACS Nano* **2017**, *11* (10), 9869–9876.
- (3) Lan, S.; Li, W.; Wang, S.; Li, J.; Wang, J.; Wang, H.; Luo, H.; Li, D. Vapor-phase growth of CsPbBr₃ microstructures for highly efficient pure green light emission. *Adv. Opt. Mater.* **2019**, *7* (2), 1801336.
- (4) Xing, J.; Liu, X. F.; Zhang, Q.; Ha, S. T.; Yuan, Y. W.; Shen, C.; Sum, T. C.; Xiong, Q. Vapor phase synthesis of organometal halide perovskite nanowires for tunable room-temperature nanolasers. *Nano Lett.* **2015**, *15* (7), 4571–4577.
- (5) Ščajev, P.; Aleksiejūnas, R.; Miasojedovas, S.; Nargelas, S.; Inoue, M.; Qin, C.; Matsushima, T.; Adachi, C.; Jursėnas, S. Two regimes of carrier diffusion in vapor-deposited lead-halide perovskites. *J. Phys. Chem. C* **2017**, *121* (39), 21600–21609.
- (6) Tong, G.; Li, H.; Li, D.; Zhu, Z.; Xu, E.; Li, G.; Yu, L.; Xu, J.; Jiang, Y. Dual-phase CsPbBr₃-CsPb₂Br₅ perovskite thin films via vapor deposition for high-performance rigid and flexible photodetectors. *Small* **2018**, *14* (7), 1702523.
- (7) Wang, Y.; Guan, X.; Li, D.; Cheng, H.; Duan, X.; Lin, Z.; Duan, X. Chemical vapor deposition growth of single-crystalline cesium lead halide microplatelets and heterostructures for optoelectronic applications. *Nano Res.* **2017**, *10* (4), 1223–1233.
- (8) Li, H.; Cao, J.; Zheng, W.; Chen, Y.; Wu, D.; Dang, W.; Wang, K.; Peng, H.; Liu, Z. Controlled synthesis of topological insulator nanoplate arrays on mica. *J. Am. Chem. Soc.* **2012**, *134* (14), 6132–6135.
- (9) Dang, W.; Peng, H.; Li, H.; Wang, P.; Liu, Z. Epitaxial heterostructures of ultrathin topological insulator nanoplate and graphene. *Nano Lett.* **2010**, *10* (8), 2870–2876.
- (10) Ha, S. T.; Liu, X.; Zhang, Q.; Giovanni, D.; Sum, T. C.; Xiong, Q. Synthesis of organic-inorganic lead halide perovskite nanoplatelets: towards high-performance perovskite solar cells and optoelectronic devices. *Adv. Opt. Mater.* **2014**, *2* (9), 838–844.
- (11) Liu, C.; Zhang, J.; Chen, Y.; Jing, P.; Zhang, L.; Zhao, H.; Fu, X.; Wang, L. Luminescence lifetime enhanced by exciton-plasmon couple in hybrid CsPbBr₃ perovskite/Pt nanostructure. *Mater. Res. Express* **2018**, *5* (2), 025014.
- (12) Shi, Z.; Li, S.; Li, Y.; Ji, H.; Li, X.; Wu, D.; Xu, T.; Chen, Y.; Tian, Y.; Zhang, Y.; Shan, C.; Du, G. Strategy of solution-processed all-inorganic heterostructure for humidity/temperature-stable perovskite quantum dot light-emitting diodes. *ACS Nano* **2018**, *12* (2), 1462–1472.
- (13) Wang, Y.; Chen, K.; Hao, H.; Yu, G.; Zeng, B.; Wang, H.; Zhang, F.; Wu, L.; Li, J.; Xiao, S.; He, J.; Zhang, Y.; Zhang, H. Engineering ultrafast charge transfer in a bismuthene/perovskite nanohybrid. *Nanoscale* **2019**, *11* (6), 2637–2643.

- (14) Sasaki, H.; Kamata, N.; Honda, Z.; Yasuda, T. Improved thermal stability of CsPbBr₃ quantum dots by ligand exchange and their application to light-emitting diodes. *Appl. Phys. Express* **2019**, *12* (3), 035004.
- (15) Begum, R.; Parida, M. R.; Abdelhady, A. L.; Murali, B.; Alyami, N. M.; Ahmed, G. H.; Hedhili, M. N.; Bakr, O. M.; Mohammed, O. F. Engineering interfacial charge transfer in CsPbBr₃ perovskite nanocrystals by heterovalent doping. *J. Am. Chem. Soc.* **2017**, *139* (2), 731–737.
- (16) Li, C.; Zang, Z.; Han, C.; Hu, Z.; Tang, X.; Du, J.; Leng, Y.; Sun, K. Highly compact CsPbBr₃ perovskite thin films decorated by ZnO nanoparticles for enhanced random lasing. *Nano Energy* **2017**, *40*, 195–202.
- (17) Ye, S.; Yan, W.; Zhao, M.; Peng, X.; Song, J.; Qu, J. Low-saturation-intensity, high-photostability, and high-resolution STED nanoscopy assisted by CsPbBr₃ quantum dots. *Adv. Mater.* **2018**, *30* (23), 1800167.
- (18) Imran, M.; Di Stasio, F.; Dang, Z.; Canale, C.; Khan, A. H.; Shamsi, J.; Brescia, R.; Prato, M.; Manna, L. Colloidal synthesis of strongly fluorescent CsPbBr₃ nanowires with width tunable down to the quantum confinement regime. *Chem. Mater.* **2016**, *28* (18), 6450–6454.
- (19) Hu, F.; Luan, Y.; Scott, M. E.; Yan, J.; Mandrus, D. G.; Xu, X.; Fei, Z. Imaging exciton–polariton transport in MoSe₂ waveguides. *Nat. Photon.* **2017**, *11* (6), 356–360.